

Article

# Morphology-Dependent Catalytic Activity of Ru/CeO<sub>2</sub> in Dry Reforming of Methane

Lulu He <sup>1</sup>, Yuanhang Ren <sup>1</sup>, Yingyi Fu <sup>1</sup>, Bin Yue <sup>1,\*</sup>, Shik Chi Edman Tsang <sup>2</sup> and Heyong He <sup>1,\*</sup>

<sup>1</sup> Department of Chemistry and Shanghai Key Laboratory of Molecular Catalysis and Innovative Materials, Collaborative Innovation Center of Chemistry for Energy Materials, Fudan University, Shanghai 200438, China; 14110220027@fudan.edu.cn (L.H.); yuanhangren@fudan.edu.cn (Y.R.); 13110220046@fudan.edu.cn (Y.F.)

<sup>2</sup> Wolfson Catalysis Centre, Department of Chemistry, University of Oxford, Oxford OX1 3QR, UK; edman.tsang@chem.ox.ac.uk

\* Correspondence: yuebin@fudan.edu.cn (B.Y.); heyonghe@fudan.edu.cn (H.H.); Tel.: +86-21-3124-3916 (H.H.); Fax: +86-21-3124-5572 (H.H.)

Academic Editors: Robert Raja, Matthew E. Potter and Stephanie Chapman

Received: 31 December 2018; Accepted: 29 January 2019; Published: 1 February 2019



**Abstract:** Three morphology-controlled CeO<sub>2</sub>, namely nanorods (NRs), nanocubes (NCs), and nanopolyhedra (NPs), with different mainly exposed crystal facets of (110), (100), and (111), respectively, have been used as supports to prepare Ru (3 wt.%) nanoparticle-loaded catalysts. The catalysts were characterized by H<sub>2</sub>-temperature programmed reduction (H<sub>2</sub>-TPR), CO-temperature programmed desorption (CO-TPD), N<sub>2</sub> adsorption-desorption, X-ray diffraction (XRD), Raman spectroscopy, X-ray photoelectron spectroscopy (XPS), transmission electron microscopy (TEM), and high-resolution transmission electron microscopy (HRTEM) and energy-dispersive X-ray spectroscopy (XDS). The characterization results showed that CeO<sub>2</sub>-NRs, CeO<sub>2</sub>-NCs, and CeO<sub>2</sub>-NPs mainly expose (110), (100) and (111) facets, respectively. Moreover, CeO<sub>2</sub>-NRs and CeO<sub>2</sub>-NCs present higher oxygen vacancy concentration than CeO<sub>2</sub>-NPs. In the CO<sub>2</sub> reforming of methane reaction, Ru/CeO<sub>2</sub>-NR and Ru/CeO<sub>2</sub>-NC catalysts showed better catalytic performance than Ru/CeO<sub>2</sub>-NPs, indicating that the catalysts with high oxygen vacancy concentration are beneficial for promoting catalytic activity.

**Keywords:** carbon dioxide; methane; CeO<sub>2</sub>; crystal facets; dry reforming

## 1. Introduction

As one of the most important emissions of modern industry and life, CO<sub>2</sub> has attracted great attention for its influence on global warming [1–3]. Many efforts have been made by governments around the world to depress the emission of CO<sub>2</sub> [4,5]. Actually, the use of CO<sub>2</sub> as a type of C1 resource for further chemical industry is also an efficient way to solve the problem [5,6]. As another important greenhouse gas, CH<sub>4</sub> exists extensively in natural resources. However, the current obstacle of the application of CH<sub>4</sub> is the activation of CH<sub>4</sub> due to its stable structure [7–9]. Thus, the studies of various reforming reactions have important industrial values and scientific significance in the application of CH<sub>4</sub>. Dry reforming of methane attracted more attention in recent years because this reaction could eliminate both greenhouse gases, CO<sub>2</sub> and CH<sub>4</sub>, simultaneously. Furthermore, the products H<sub>2</sub> and CO (syngas) of the reaction have a low H<sub>2</sub>/CO molar ratio of nearly 1, which is more suitable for the subsequent chemical industrial processes [10–12].

For the methane dry reforming reaction, many kinds of catalysts have been widely studied by loading active metals on different supports. Ni, Co, Rh, Ru, Pd, Ir, and Pt have been studied for methane dry reforming reaction in recently years [7,13–15]. Ni- and Co-based catalysts attracted more

interest due to their lower price than noble metals. However, the sintering and coking problems along with the poor activity of the catalysts at relatively low temperature are difficult to solve. As a result, the study of noble metals in methane dry reforming is of great significance and the Rh- or Ru-based catalysts have been considered to have better activity and stability [15–17]. On the other hand, a lot of work has focused on the influence of the different metal oxide supports, such as  $\text{SiO}_2$ ,  $\gamma\text{-Al}_2\text{O}_3$ ,  $\text{MgO}$ ,  $\text{ZrO}_2$ ,  $\text{La}_2\text{O}_3$ , and  $\text{TiO}_2$  [18–24]. These studies showed that the supports played an important role in their catalytic activity. The supports may not only offer various textures to disperse the active metal components, but also interact strongly with the active species. The interaction between supports and active metals influence on the structure of catalysts, the particle sizes, and the dispersion of active sites consequently influences the catalytic activity of the catalysts [25]. For example, Wang et al. found that the catalytic performance of a series of catalysts for methane dry reforming reaction was related to the redox properties of the supports [26].

$\text{CeO}_2$  is a unique metal oxide due to its low redox potential and high oxygen vacancy mobility, which could have a strong interaction with the active metals [27–29]. In recent years,  $\text{CeO}_2$  has been widely used as a catalyst promoter or support for various reactions, such as dry reforming of methane, partial oxidation of methane, dry reforming of propane, and steam reforming of ethanol [30–34]. The studies indicate that the existence of  $\text{CeO}_2$  in catalysts benefits their resistance to carbon deposition, because the coke on the catalyst could be removed by reacting with the oxygen species on the surface of  $\text{CeO}_2$ . Thus, the release of oxygen species is a crucial process for  $\text{CeO}_2$ -based catalysts. Generally, the surface energy of metal oxides is strongly related with their microstructures, and there are evident differences in surface energy among the faces with various indices of the crystallographic plane. The catalytic activity of shape-dependent  $\text{CeO}_2$ -supported active metal is obviously different [35–40]. Therefore, it is reasonable to believe that the use of  $\text{CeO}_2$  supports specific exposed crystal facets may influence the catalytic behavior of the catalyst in dry reforming of methane.

In this work, we have prepared a series of  $\text{CeO}_2$  nanorods ( $\text{CeO}_2$ -NRs), nanocubes ( $\text{CeO}_2$ -NCs), and nanopolyhedra ( $\text{CeO}_2$ -NPs) with dominant specific crystal facets (110), (100), and (111), respectively. These morphology-controlled  $\text{CeO}_2$  were used as supports for Ru as a catalytic active component through precipitation and deposition methods. The catalysts were characterized, and their catalytic behavior for dry reforming of methane was studied. In particular, the influence of the exposed crystal facets of the  $\text{CeO}_2$  supports on the catalytic activities was investigated in detail.

## 2. Results and Discussion

### 2.1. Catalyst Characterization

#### 2.1.1. TEM and High-Resolution Transmission Electron Microscopy (HRTEM) Analysis

Figure 1 shows the TEM and HRTEM images of the  $\text{CeO}_2$  supports and Ru/ $\text{CeO}_2$  catalysts. In Figure 1a–f, three  $\text{CeO}_2$  samples show different morphologies.  $\text{CeO}_2$ -NRs with the rod-like morphology in Figure 1a,d exhibit a uniform diameter of ca. 10 nm with two obvious interplanar spacings of 0.19 and 0.27 nm, corresponding to the (220) and (200) lattice fringes, respectively. The shape of  $\text{CeO}_2$ -NRs indicates that the nanorods grow along the (110) direction. Figure 1b,e shows that  $\text{CeO}_2$ -NCs possess the cubic morphology with a size of around 10–50 nm and clear (200) lattice fringes with the interplanar spacing of 0.27 nm. Figure 1c,f shows  $\text{CeO}_2$ -NPs in the size range of 10–20 nm and (111) and (200) lattice fringes corresponding to the interplanar spacing of 0.31 and 0.27 nm, respectively [41]. HRTEM results show that only the (100) facet exists in the  $\text{CeO}_2$ -NCs, whereas the (110) and (111) facets are the mainly exposed planes for  $\text{CeO}_2$ -NRs and  $\text{CeO}_2$ -NPs, respectively. Figure 1g–i shows TEM images of 3% Ru/ $\text{CeO}_2$  catalysts. It can be seen that the morphology of the supports remains after the loading of Ru species and no large aggregation was observed, indicating the high dispersion of the Ru species. The distribution of Ce and Ru was evaluated by EDS analysis. The EDS results are shown in Figures S1–S3 for the Ru/ $\text{CeO}_2$ -NRs, Ru/ $\text{CeO}_2$ -NCs, and Ru/ $\text{CeO}_2$ -NPs,

respectively. The elemental mapping results also indicate that Ru species are highly dispersed on the surface of CeO<sub>2</sub> supports.

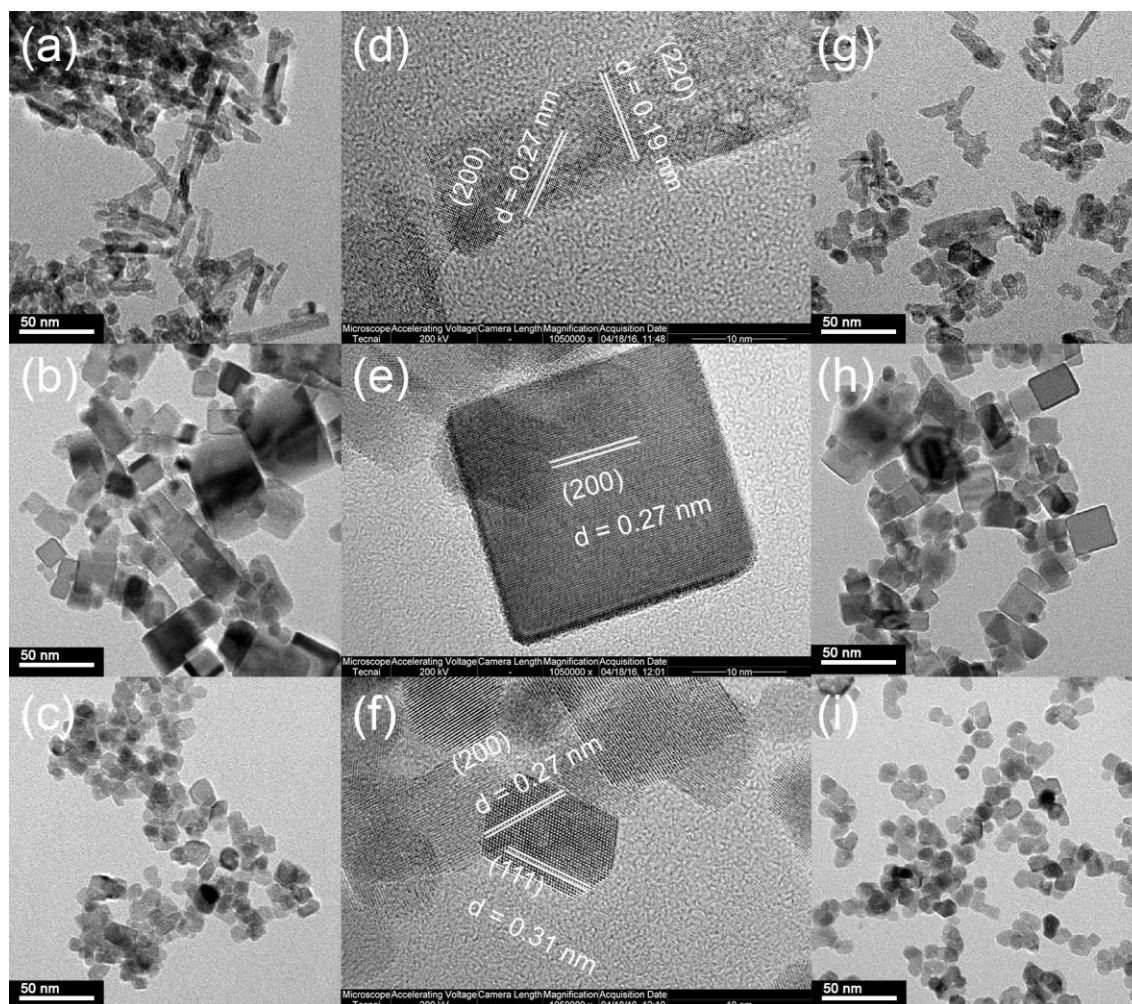


**Figure 1.** TEM images of (a) CeO<sub>2</sub>-NRs, (b) CeO<sub>2</sub>-NCs, and (c) CeO<sub>2</sub>-NPs; high-resolution transmission electron microscopy (HRTEM) images of (d) CeO<sub>2</sub>-NRs, (e) CeO<sub>2</sub>-NCs, and (f) CeO<sub>2</sub>-NPs; TEM images of (g) Ru/CeO<sub>2</sub>-NRs, (h) Ru/CeO<sub>2</sub>-NCs, and (i) Ru/CeO<sub>2</sub>-NPs.

### 2.1.2. X-ray Diffraction

Figure 2 shows the XRD patterns of CeO<sub>2</sub> samples with different exposed facets and their corresponding 3% Ru/CeO<sub>2</sub> catalysts. The peaks of CeO<sub>2</sub>-NRs, CeO<sub>2</sub>-NCs, and CeO<sub>2</sub>-NPs at 28.7°, 33.2°, 47.6°, 56.5°, 59.1°, 69.4°, 76.6°, and 79.2° are assigned to the diffractions of (111), (200), (220), (311), (222), (400), (311), and (420) of CeO<sub>2</sub> indexed to the face-centered cubic fluorite structure with space group *Fm-3m* (JCPDS 34-0394). The crystalline sizes of different samples calculated by Scherrer formula are listed in Table 1. The results are consistent with TEM images. The diffraction peak positions of the three CeO<sub>2</sub> supports are nearly the same, but their relative intensities are different. The different ratios of  $(I_{(200)}/I_{(111)} + I_{(220)}/I_{(111)})$  as 1.00, 1.02, and 0.82 for CeO<sub>2</sub>-NRs, CeO<sub>2</sub>-NCs, and CeO<sub>2</sub>-NPs, respectively, show that the (111) facet exposure in the nanopolyhedra is higher than that in nanorods and nanocubes, which are consistent with the TEM and HRTEM analysis [39]. The XRD patterns of different Ru/CeO<sub>2</sub> catalysts are shown in Figure 2d–f, and no significant change of the diffractions of CeO<sub>2</sub> can be found, suggesting that the structure of CeO<sub>2</sub> supports remains. It is worth to note that from the inductively coupled plasma atomic emission spectrometer (ICP-AES) results (Table 1), Ru/CeO<sub>2</sub> samples show close Ru loading to the feeding value of 3 wt.% despite some weight loss.



No new diffraction assigned to Ru species appears in the XRD patterns, indicating the high dispersion of metal species on the support. The Ru dispersion calculated from CO-TPD shows that the Ru species are highly dispersed on the CeO<sub>2</sub> supports. Ru/CeO<sub>2</sub>-NRs and Ru/CeO<sub>2</sub>-NCs display higher Ru dispersion (54% and 59%, respectively) than that of Ru/CeO<sub>2</sub>-NPs (35.0%) (Table 1). The results are consistent with the EDS mappings results (Supplementary Materials).

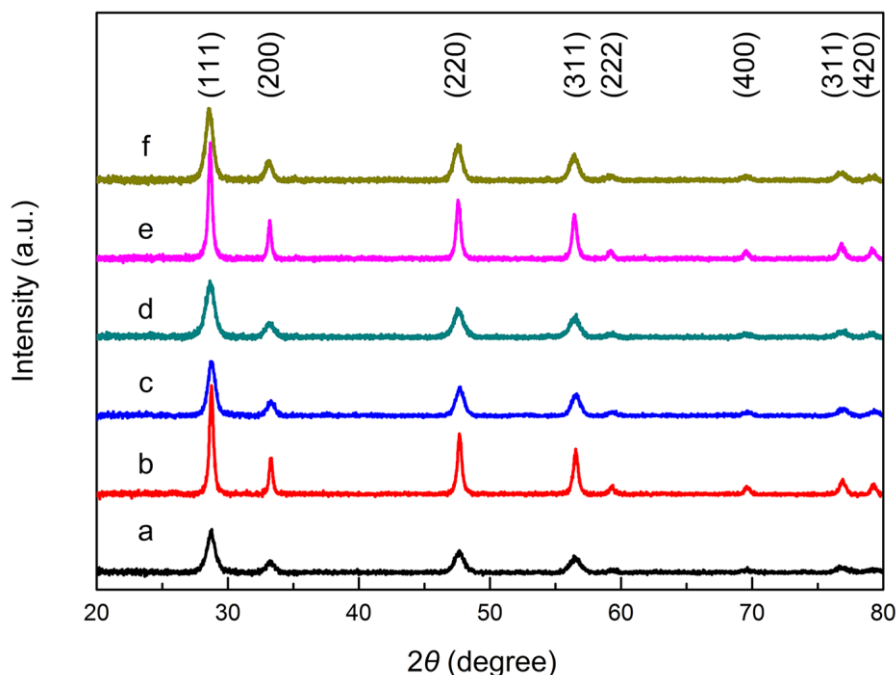


**Figure 2.** XRD patterns of (a) CeO<sub>2</sub>-NRc, (b) CeO<sub>2</sub>-NCs, (c) CeO<sub>2</sub>-NPs, (d) Ru/CeO<sub>2</sub>-NRs, (e) Ru/CeO<sub>2</sub>-NCs, and (f) Ru/CeO<sub>2</sub>-NPs.

**Table 1.** Physical properties of various samples.

Sample	Specific Surface Area <sup>a</sup> (m <sup>2</sup> ·g <sup>-1</sup> )	Particle Size <sup>b</sup> (nm)	Mean Sizes <sup>c</sup> (nm)	Ru <sup>d</sup> (wt.%)	Ru Dispersion <sup>e</sup> (%)
CeO <sub>2</sub> -NRs	87.1	(8 ± 2) × (50 – 100)	13.6	-	-
CeO <sub>2</sub> -NCs	31.7	26 ± 15	23.0	-	-
CeO <sub>2</sub> -NPs	67.4	13 ± 5	13.9	-	-
Ru/CeO <sub>2</sub> -NRs	84.9	(7 ± 3) × (20 – 100)	12.1	2.4	54
Ru/CeO <sub>2</sub> -NCs	30.1	24 ± 15	23.6	2.4	59
Ru/CeO <sub>2</sub> -NPs	65.8	12 ± 5	13.7	2.3	35

<sup>a</sup> Surface area determined from N<sub>2</sub> isotherm. <sup>b</sup> Calculated for about 100 nanoparticles from the TEM images.

<sup>c</sup> Estimated by Scherrer equation, applied to the (111) reflection on fluorite CeO<sub>2</sub>. <sup>d</sup> Analyzed by inductively coupled plasma atomic emission spectrometer (ICP-AES). <sup>e</sup> calculated based on the CO-TPD results.

### 2.1.3. N<sub>2</sub> Adsorption–Desorption

The N<sub>2</sub> adsorption–desorption characterization was performed at 77 K to study the textural properties of CeO<sub>2</sub> supports and Ru/CeO<sub>2</sub> catalysts. The Brunauer–Emmett–Teller (BET) surface areas of CeO<sub>2</sub>-NRs, CeO<sub>2</sub>-NCs, and CeO<sub>2</sub>-NPs and their corresponding Ru-supported catalysts, Ru/CeO<sub>2</sub>-NRs, Ru/CeO<sub>2</sub>-NCs, and Ru/CeO<sub>2</sub>-NPs are 87.1, 31.7, 67.4, 84.9, 30.1, and 65.8 m<sup>2</sup>·g<sup>-1</sup>, respectively. As shown in Table 1, the surface areas of pure CeO<sub>2</sub>-NRs and CeO<sub>2</sub>-NPs are higher than those of CeO<sub>2</sub>-NCs, which is mainly because of smaller particle sizes of the former compared to the latter. The surface areas and particle sizes are merely changed after the addition of Ru species with low loading. It is well known that the surface area has an influence on the catalytic activity for

many reactions, and the catalysts with a large surface area would be beneficial to enhance the catalytic activity. However, for some reaction over ceria-based catalysts, the surface area is not the crucial factor based on the previous research [33,36].

#### 2.1.4. H<sub>2</sub>-Temperature Programmed Reduction

The H<sub>2</sub>-temperature programmed reduction (H<sub>2</sub>-TPR) measurements were performed to clarify the reduction characteristics of CeO<sub>2</sub> supports and supported Ru/CeO<sub>2</sub> catalysts. As shown in Figure 3a, two reduction peaks appear in the temperature range of 250–900 °C for three CeO<sub>2</sub> supports with different exposed facets. The first peak below 600 °C is due to the reduction of Ce<sup>4+</sup> to Ce<sup>3+</sup> on the CeO<sub>2</sub> surface with oxygen vacancy, and the second peak is the reduction of Ce<sup>4+</sup> to Ce<sup>3+</sup> inside the bulk CeO<sub>2</sub> [27,40]. After loading the Ru species on the supports, the reduction peak changed significantly. The presence of two sets of peaks at 30–110 °C and 110–200 °C indicates Ru species exist in two different states. The reduction peaks at low temperature are usually assigned to the adsorbed oxygen and well-dispersed Ru species interacting strongly with the CeO<sub>2</sub> supports [42]. From the previous research, the surface energies ( $\gamma$ ) associated with different crystallographic planes are usually different, and a general sequence is  $\gamma(111) < \gamma(100) < \gamma(110)$  [43,44]. Thus, the order of reduction temperature of all catalysts in the range of 30–110 °C is Ru/CeO<sub>2</sub>-NRs < Ru/CeO<sub>2</sub>-NCs < Ru/CeO<sub>2</sub>-NPs, which agrees with the energy order of different facets. The reduction peaks at a relatively high temperature are assigned to the Ru species interacting weakly with CeO<sub>2</sub> supports and the surface oxygen of CeO<sub>2</sub>. It has been reported that the hydrogen consumption is 178–188  $\mu\text{mol}\cdot\text{g}^{-1}$  for the reaction of  $\text{RuO}_2 + 2\text{H}_2 \rightarrow \text{Ru}^0 + 2\text{H}_2\text{O}$  [42]. The total H<sub>2</sub> consumption calculated by integrating the peaks is  $\sim 754 \mu\text{mol}\cdot\text{g}^{-1}$  for Ru/CeO<sub>2</sub>-NRs,  $\sim 710 \mu\text{mol}\cdot\text{g}^{-1}$  for Ru/CeO<sub>2</sub>-NCs, and  $\sim 638 \mu\text{mol}\cdot\text{g}^{-1}$  for Ru/CeO<sub>2</sub>-NPs. The high hydrogen consumption of three catalysts should result from the reduction of a large amount of surface oxygen of CeO<sub>2</sub> due to the existence of Ru–O–Ce. The low hydrogen consumption of Ru/CeO<sub>2</sub>-NPs indicates that the Ru species have a weak interaction with CeO<sub>2</sub> support compared to those of Ru/CeO<sub>2</sub>-NRs and Ru/CeO<sub>2</sub>-NCs.

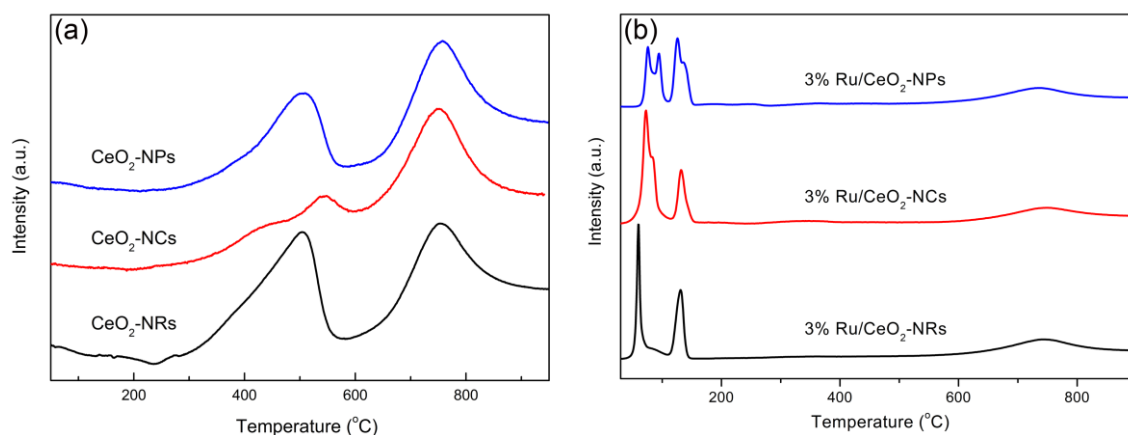


**Figure 3.** H<sub>2</sub>-temperature programmed reduction (H<sub>2</sub>-TPR) curves of (a) CeO<sub>2</sub> samples (b) Ru/CeO<sub>2</sub> samples.

#### 2.1.5. Raman Spectroscopy

Figure 4 shows Raman spectra of CeO<sub>2</sub> supports and Ru/CeO<sub>2</sub> catalysts. All three CeO<sub>2</sub> supports with different morphologies exhibit a strong peak at around 461 cm<sup>-1</sup>, which is assigned to the vibration model (F<sub>2g</sub>) of the CeO<sub>2</sub> fluorite phase. Additionally, the other three weak peaks at 257, 594, and 1170 cm<sup>-1</sup> are assigned to second-order transverse acoustic (2TA) mode, defect-induced (D) mode, and second-order longitudinal optical (2LO) mode, respectively [35–38,45]. The relative intensity of  $I_{(594+1170)}/I_{461}$  reflects the intrinsic concentration of defect sites on CeO<sub>2</sub> supports, such as oxygen vacancies [38,46]. The calculation results show that the concentration of vacancy sites decreases in the

following order of  $\text{CeO}_2\text{-NRs} > \text{CeO}_2\text{-NCs} > \text{CeO}_2\text{-NPs}$  (Table 2). This is because the formation energy of vacancy is in a reversed order of surface energies on different facets [43]. After the loading of the Ru species, two new peaks appear at 694 and 968  $\text{cm}^{-1}$  in addition to the peaks of  $\text{CeO}_2$  supports, which are ascribed to the formation of the Ru–O–Ce bond between metal oxides and supports [38,40]. The relative intensity ratio of  $I_{(694+968)}/I_{461}$  implies that the interaction between Ru and  $\text{CeO}_2$  supports on Ru/ $\text{CeO}_2\text{-NR}$  and Ru/ $\text{CeO}_2\text{-NC}$  samples is stronger than that on the Ru/ $\text{CeO}_2\text{-NP}$  sample [38], in accordance with the TPR results.

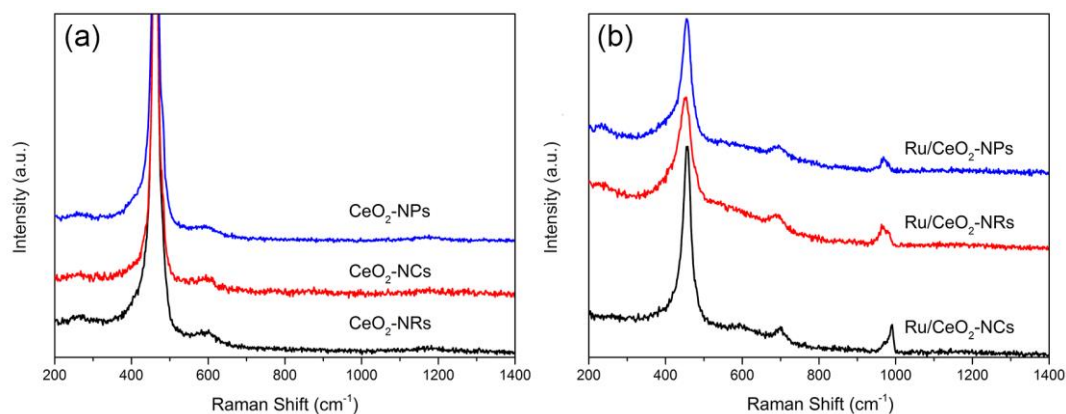


**Figure 4.** Raman spectra of (a)  $\text{CeO}_2$  samples (b) Ru/ $\text{CeO}_2$  samples.

**Table 2.** Raman spectral data of  $\text{CeO}_2$  and Ru/ $\text{CeO}_2$  samples.

Sample	$I_{(594 + 1170)}/I_{461}$	$I_{(694 + 968)}/I_{461}$
$\text{CeO}_2\text{-NRs}$	0.116	-
$\text{CeO}_2\text{-NCs}$	0.102	-
$\text{CeO}_2\text{-NPs}$	0.057	-
Ru/ $\text{CeO}_2\text{-NRs}$	-	0.234
Ru/ $\text{CeO}_2\text{-NCs}$	-	0.187
Ru/ $\text{CeO}_2\text{-NPs}$	-	0.177

#### 2.1.6. X-ray Photoelectron Spectroscopy (XPS)

Figure 5 shows Ru 3d XPS spectra of Ru/ $\text{CeO}_2$  samples before  $\text{H}_2$  reduction. The Ru XPS results of Ru/ $\text{CeO}_2\text{-NCs}$  and Ru/ $\text{CeO}_2\text{-NPs}$  show three peaks around 277.5, 281.4, and 284.8 eV, which are assigned to  $\text{Ru}^0$ ,  $\text{Ru}^{4+}$ , and  $\text{Ru}^{6+}$ , respectively. The Ru/ $\text{CeO}_2\text{-NRs}$  only exhibit two Ru species, which could be assigned to  $\text{Ru}^{6+}$  and  $\text{Ru}^{4+}$  [35,38]. Moreover, the content of  $\text{Ru}^{4+}$  follows the order: Ru/ $\text{CeO}_2\text{-NRs} > \text{Ru}/\text{CeO}_2\text{-NCs} > \text{Ru}/\text{CeO}_2\text{-NPs}$  (Table 3). The  $\text{Ru}^{4+}$  ions may insert into the surface lattice of  $\text{CeO}_2$  to increase of oxygen vacancy concentration on the  $\text{CeO}_2$  support [38]. This effect leads to the high concentration of surface oxygen vacancies for Ru/ $\text{CeO}_2\text{-NRs}$  and Ru/ $\text{CeO}_2\text{-NCs}$  catalysts, and, on the other hand, the decrease of the aggregation of  $\text{RuO}_2$  particles.

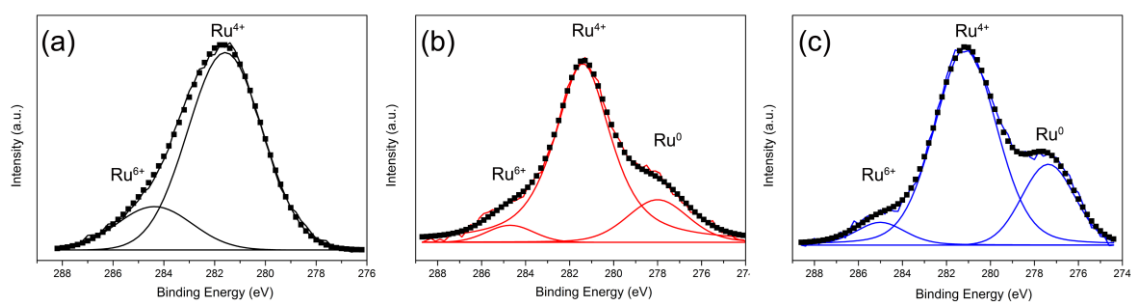
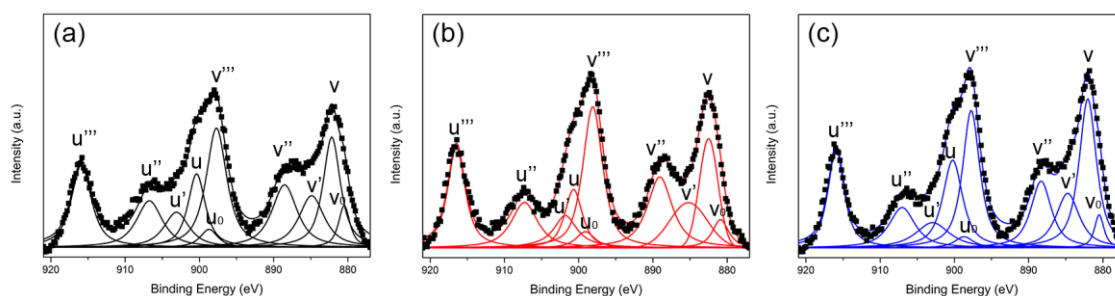


**Figure 5.** Ru 3d X-ray photoelectron spectroscopy (XPS) spectra of (a) Ru/CeO<sub>2</sub>-NRs, (b) Ru/CeO<sub>2</sub>-NCs, and (c) Ru/CeO<sub>2</sub>-NPs.

**Table 3.** XPS data of Ru/CeO<sub>2</sub>-NR, Ru/CeO<sub>2</sub>-NC, and Ru/CeO<sub>2</sub>-NP samples.

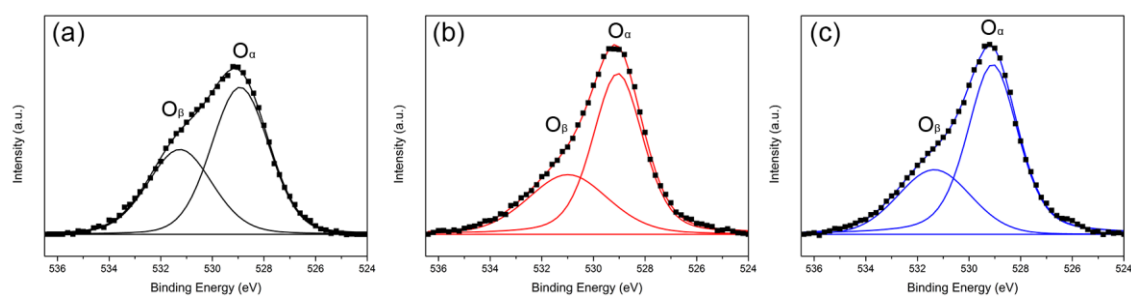
Samples	Ru <sup>4+</sup> (%)	Ce <sup>3+</sup> /(Ce <sup>3+</sup> + Ce <sup>4+</sup> ) (%)	O <sub>β</sub> /O <sub>α</sub>
Ru/CeO <sub>2</sub> -NRs	80.9	22.8	0.40
Ru/CeO <sub>2</sub> -NCs	78.9	21.1	0.36
Ru/CeO <sub>2</sub> -NPs	22.4	19.8	0.32

Figure 6 shows the Ce 3d XPS spectra of three Ru/CeO<sub>2</sub> samples. There are ten peaks resulting from the pairs of spin orbit doublets, which can be identified through deconvolution. The four peaks around 880.6 (v<sub>0</sub>), 884.4 (v'), 898.8 (u<sub>0</sub>), and 901.0 eV (u') are assigned to Ce<sup>3+</sup> species, and six peaks around 882.2 (v), 888.6 (v''), 898.3 (v'''), 900.7 (u), 907.7 (u''), and 916.2 eV (u''') are assigned to Ce<sup>4+</sup> species [36–38,47]. The intensity ratio of Ce<sup>3+</sup>/(Ce<sup>3+</sup> + Ce<sup>4+</sup>) is 22.8%, 21.1%, and 19.8% for Ru/CeO<sub>2</sub>-NRs, Ru/CeO<sub>2</sub>-NCs, and Ru/CeO<sub>2</sub>-NPs, respectively. The appearance of Ce<sup>3+</sup> species leads to the formation of oxygen vacancy on the CeO<sub>2</sub> surface. The high concentration of Ce<sup>3+</sup> on the surface reflects the high concentration of surface oxygen vacancies, which benefits the activation and conversion of reactants in dry reforming of methane reaction [40].



**Figure 6.** Ce 3d XPS spectra of (a) Ru/CeO<sub>2</sub>-NRs, (b) Ru/CeO<sub>2</sub>-NCs, and (c) Ru/CeO<sub>2</sub>-NPs.

Figure 7 shows O 1s XPS spectra of Ru/CeO<sub>2</sub> samples. All three samples mainly exist in two peaks corresponding to two kinds of oxygen species. The peak around 529 eV is ascribed to the oxygen species inside of the CeO<sub>2</sub> lattice, marked as the O<sub>α</sub> species, and the peak around 531 eV marked O<sub>β</sub> species is mainly ascribed to low coordination oxygen defects on the surface [36,48]. As shown in Table 3, Ru/CeO<sub>2</sub>-NRs have the highest O<sub>β</sub>/O<sub>α</sub> ratio and Ru/CeO<sub>2</sub>-NPs have the lowest O<sub>β</sub>/O<sub>α</sub> ratio. The O<sub>β</sub>/O<sub>α</sub> ratio estimated through deconvolution shows that the content of surface oxygen defects on CeO<sub>2</sub> is morphology-dependent.



**Figure 7.** O 1s XPS spectra of (a) Ru/CeO<sub>2</sub>-NRs, (b) Ru/CeO<sub>2</sub>-NCs, and (c) Ru/CeO<sub>2</sub>-NPs.

## 2.2. Catalytic Performance for the Dry Reforming of Methane

The catalytic performance of three CeO<sub>2</sub>-supported Ru catalysts in the dry reforming of methane under the reaction temperature of 500 °C and 650 °C is shown in Figures 8 and 9. Compared to high CO<sub>2</sub> conversion, low CH<sub>4</sub> conversion is due to the simultaneous occurrence of a reverse water-gas shift reaction. Moreover, the catalytic activities for all three catalysts remain relatively stable after a 240-min reaction. The conversion trends of CO<sub>2</sub> and CH<sub>4</sub> are followed by Ru/CeO<sub>2</sub>-NRs (26.5% of CO<sub>2</sub> and 12.3% of CH<sub>4</sub>) ≈ Ru/CeO<sub>2</sub>-NCs (26.0% of CO<sub>2</sub> and 13.6% of CH<sub>4</sub>) > Ru/CeO<sub>2</sub>-NPs (19.3% of CO<sub>2</sub> and 6.2% of CH<sub>4</sub>) after a 240-min reaction process. Both CO<sub>2</sub> and CH<sub>4</sub> conversions increase for all three catalysts when increasing the temperature to 650 °C (Figure 9). The conversions of CO<sub>2</sub> and CH<sub>4</sub> over Ru/CeO<sub>2</sub>-NR and Ru/CeO<sub>2</sub>-NC samples are much higher than those for Ru/CeO<sub>2</sub>-NPs.

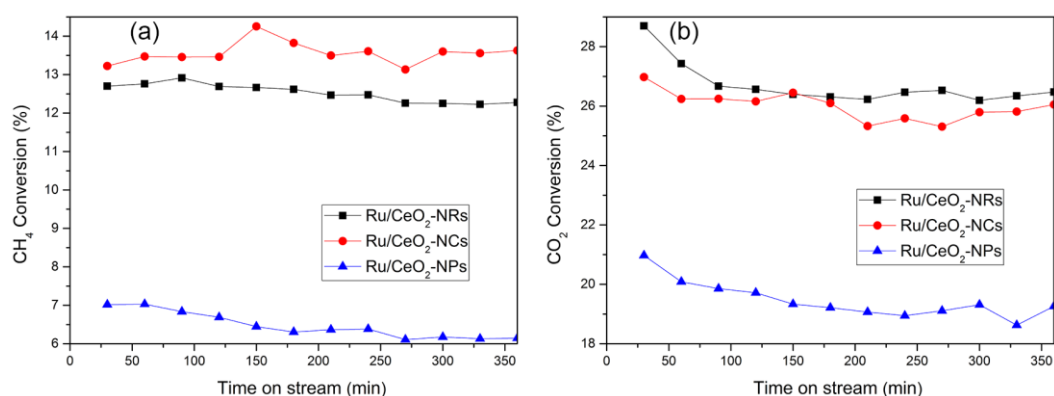


**Figure 8.** The CH<sub>4</sub> conversion (a) and CO<sub>2</sub> conversions (b) of three Ru/CeO<sub>2</sub> samples versus time at 500 °C.

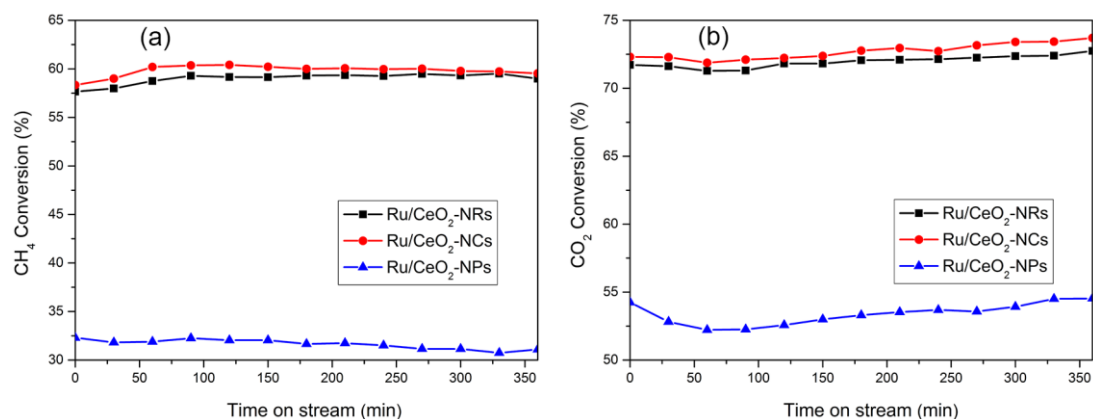


**Figure 9.** The CH<sub>4</sub> conversion (a) and CO<sub>2</sub> conversions (b) of three Ru/CeO<sub>2</sub> samples versus time at 650 °C.



From the above results, CeO<sub>2</sub> exposed with a high energy facet of (110) and (100) have a high catalytic activity in the methane dry reforming reaction. This is due to the strong interaction between Ru species and supports exposed (110) and (100) facets, and the (110) and (100) facets on the CeO<sub>2</sub> with high oxygen vacancy concentration benefit the activation of CO<sub>2</sub> during the reaction.

### 3. Experimental Section

#### 3.1. Preparation of CeO<sub>2</sub> Samples

Morphology-controlled CeO<sub>2</sub> samples were synthesized using the hydrothermal method. For the preparation of CeO<sub>2</sub>-NCs and CeO<sub>2</sub>-NPs, 1.82 g of Ce(NO<sub>3</sub>)<sub>3</sub>·6H<sub>2</sub>O was dissolved in 40 mL of distilled water and 16.8 g of NaOH for CeO<sub>2</sub>-NCs or 0.33 g of NaOH for CeO<sub>2</sub>-NPs were dissolved in 30 mL of distilled water. The Ce(NO<sub>3</sub>)<sub>3</sub> solution was added into the NaOH solution dropwisely under stirring and stirred for further 30 min to form a milky slurry. Then, the milky slurry was transferred into a 100-mL stainless steel autoclave and hydrothermally treated at 180 °C for 24 h. After the autoclave was cooled to room temperature naturally, the precipitates were separated by centrifugation, washed with distilled water thoroughly, dried at 60 °C for 12 h, and calcined at 500 °C with a heating rate of 1 °C min<sup>-1</sup> from room temperature for 4 h to obtain the CeO<sub>2</sub>-NCs and CeO<sub>2</sub>-NPs. The synthesis procedure of CeO<sub>2</sub>-NRs was the same as that of CeO<sub>2</sub>-NCs, except that the hydrothermal treatment temperature was 100 °C.

#### 3.2. Preparation of Ru/CeO<sub>2</sub> Catalysts

The Ru/CeO<sub>2</sub> catalysts were prepared using the precipitation and deposition method. A total of 1.0 g of CeO<sub>2</sub> was added into a 20 mL of solution containing 0.015 g of RuCl<sub>3</sub>·3H<sub>2</sub>O and stirred for 30 min. Then, 0.1 M NH<sub>3</sub>·H<sub>2</sub>O aqueous solution was added to adjust the pH of the suspension up to 8.0, and then the suspension was aged at room temperature for 3 h. The catalyst in suspension was separated by centrifugation, washed with distilled water, dried at 60 °C for 12 h, and calcined at 500 °C with a heating rate of 1 °C ·min<sup>-1</sup> from room temperature for 4 h. The loading of metal Ru in the catalysts is 3 wt.%.

#### 3.3. Catalyst Characterization

Transmission electron microscopy (TEM) and high-resolution TEM (HRTEM) images were obtained on a JEM-2011 transmission electron microscope (JOEL, Japan) and a FEI Tecnai G<sup>2</sup> F20 S-Twin field-emission transmission electron microscope (Hillsboro, OR, USA, respectively). X-ray diffraction (XRD) patterns were obtained on a Bruker D8 Advance diffractometer (Karlsruhe, Germany), using Cu K $\alpha$  radiation ( $\lambda = 1.5418 \text{ \AA}$ ) at 40 kV and 40 mA, a scanning rate of 5°·min<sup>-1</sup>, a step size of 0.02°, and a 2 $\theta$  angle ranging from 20° to 80°. The N<sub>2</sub> adsorption–desorption characterization was performed using a Micromeritics Tristar 3000 apparatus (Quantachrome, Boynton Beach, FL, USA). Prior to the adsorption measurements, the sample was outgassed at 250 °C for 3 h under vacuum. The specific surface areas were calculated using the Brunauer–Emmett–Teller (BET) method. Elemental analysis was performed on a Thermo Elemental IRIS Intrepid inductively coupled plasma atomic emission spectrometer (ICP-AES, Thermo Elemental, Waltham, MA, USA). X-ray photoelectron spectroscopy (XPS) was performed on a Versa Probe PHI 5000 instrument with Al K $\alpha$  radiation (Versa Probe, Amreica). The binding energies were calibrated using the containment carbon (C1s = 284.6 eV). H<sub>2</sub>-temperature programmed reduction (H<sub>2</sub>-TPR) was performed using a Micromeritics ChemiSorb 2720 apparatus with a thermal conductivity detector (TCD, Micromeritics, Chanhassen, MN, USA). Before measurement, 45.0 mg of sample was placed in a U-shape quartz tube and degassed under flowing He at 200 °C for 2 h, cooled to room temperature, and then switched gas to 10% H<sub>2</sub>/Ar. The sample was reduced in a stream of 10% H<sub>2</sub>/Ar (50 mL·min<sup>-1</sup>) with a heating rate of 10 °C min<sup>-1</sup> from room temperature up to 900 °C. CO-temperature programmed desorption (CO-TPD) was performed to determine the dispersion of Ru particles using a Micromeritics ChemiSorb 2720 apparatus

with TCD (Micromeritics, Chanhassen, MN, USA). The Ru:CO molar ratio in the chemisorption was taken as 1 [49]. The sample (45.0 mg) was firstly reduced in a stream of 10% H<sub>2</sub>/Ar (50 mL·min<sup>-1</sup>) at 500 °C for 2 h. Subsequently, the reduced sample was purged in He (50 mL min<sup>-1</sup>) at 500 °C for 30 min to remove excess H<sub>2</sub> and then cooled down to 40 °C for adsorption of CO for 30 min, and then gas was switched to He to keep 30 min at 40 °C to remove excess CO. Finally, the samples were heated in He with a temperature ramp of 10 °C min<sup>-1</sup>.

### 3.4. Catalytic Activity Measurements

The catalytic measurements for dry reforming of methane were carried out in a quartz tube with the inner diameter of 6 mm using a fixed-bed reactor system at atmospheric pressure. The gas flow rate was controlled by mass-flow controllers. A total of 30 mg of 40–60 mesh catalyst was mixed with 250 mg of 40–60 mesh inert quartz sand and placed into the reactor. Before the reaction, the catalyst was reduced in a flow of H<sub>2</sub> (30 mL·min<sup>-1</sup>) at 500 °C for 2 h. Then, the reaction gas mixture consisting of CO<sub>2</sub>, CH<sub>4</sub>, and N<sub>2</sub> (CO<sub>2</sub>:CH<sub>4</sub>:N<sub>2</sub> volume ratio of 1:1:3) was introduced into the reaction with the gas hourly space velocity (GHSV) of 24,000 mL·h<sup>-1</sup>·g<sup>-1</sup> (CO<sub>2</sub> + CH<sub>4</sub> + N<sub>2</sub>), and the effluent product gases were cooled in an ice-water bath and analyzed by online gas chromatography with a thermal conductivity detector (TCD) using a TDX-01 packed column. The reaction activity of the methane dry reforming reaction was tested at 500 °C and 650 °C.

## 4. Conclusions

In this work, a series of CeO<sub>2</sub> supports, CeO<sub>2</sub>-NRs, CeO<sub>2</sub>-NCs, and CeO<sub>2</sub>-NPs, with different exposed facets were synthesized via the hydrothermal method; the metal Ru was loaded on the CeO<sub>2</sub> supports as catalyst for the dry reforming of methane. The CeO<sub>2</sub>-NR and CeO<sub>2</sub>-NC supports with mainly (110) and (100) exposed facets contain higher oxygen vacancy concentration than the CeO<sub>2</sub>-NP supports with (111) exposed facets. The high energy surface structure of the CeO<sub>2</sub>-NRs and CeO<sub>2</sub>-NCs enhances the interaction between Ru and CeO<sub>2</sub>. The catalytic results of the three catalysts for dry reforming of methane are related with the surface energy of the CeO<sub>2</sub> supports and the Ru/CeO<sub>2</sub>-NR and Ru/CeO<sub>2</sub>-NC catalysts perform a higher catalytic activity than Ru/CeO<sub>2</sub>-NPs, due to the former containing higher oxygen vacancy concentration.

**Supplementary Materials:** The following are available online, Figure S1: Ce, Ru, and O mapping with EDS spectrum of the Ru/CeO<sub>2</sub>-NR catalyst. Figure S2: Ce, Ru, and O mapping with EDS spectrum of the Ru/CeO<sub>2</sub>-NC catalyst. Figure S3: Ce, Ru, and O mapping with EDS spectrum of the NRu/CeO<sub>2</sub>-NP catalyst.

**Author Contributions:** Conceptualization, B.Y. and H.H.; Data curation, Y.R. and Y.F.; Formal analysis, L.H. and Y.F.; Investigation, L.H.; Methodology, L.H. and B.Y.; Project administration, H.H.; Software, Y.R.; Supervision, H.H.; Writing—original draft, L.H.; Writing—review and editing, B.Y., S.C.E.T., and H.H.

**Funding:** The authors acknowledge the financial supports from the National Natural Science Foundation of China (91645201, 21473036 and 21673046) and the Ministry of Science and Technology (2017YFB0602204).

**Conflicts of Interest:** The authors declare no conflict of interest.

## References

1. Florides, G.A.; Christodoulides, P.; Messaritis, V. Reviewing the effect of CO<sub>2</sub> and the sun on global climate. *Renew. Sustain. Energy Rev.* **2013**, *26*, 639–651. [[CrossRef](#)]
2. Ghoniem, A.F. Needs, resources and climate change: Clean and efficient conversion technologies. *Prog. Energy Combust. Sci.* **2011**, *37*, 15–51. [[CrossRef](#)]
3. Appel, A.M.; Bercaw, J.E.; Bocarsly, A.B.; Dobbek, H.; DuBois, D.L.; Dupuis, M.; Ferry, J.G.; Fujita, E.; Hille, R.; Kenis, P.J.A.; et al. Frontiers, opportunities, and challenges in biochemical and chemical catalysis of CO<sub>2</sub> fixation. *Chem. Rev.* **2013**, *113*, 6621–6658. [[CrossRef](#)] [[PubMed](#)]
4. Abdallah, D.; Dang, V.Q.; Lourdes, F.V.; Enas, N.; Mohammad, R.M.A.-Z. Applications of fly ash for CO<sub>2</sub> capture, utilization, and storage. *J. CO<sub>2</sub> Util.* **2019**, *29*, 82–102.

5. Aresta, M.; Dibenedetto, A.; Angelini, A. The changing paradigm in CO<sub>2</sub> utilization. *J. CO<sub>2</sub> Util.* **2013**, *3–4*, 65–73. [[CrossRef](#)]
6. Kawi, S.; Kathiraser, Y.; Ni, J.; Oemar, U.; Li, Z.; Saw, E.T. Progress in synthesis of highly active and stable nickel-based catalysts for carbon dioxide reforming of methane. *ChemSusChem* **2015**, *8*, 3556–3575. [[CrossRef](#)] [[PubMed](#)]
7. Spallina, V.; Melchiori, T.; Gallucci, F.; Annaland, M.v.S. Auto-thermal reforming using mixed ion-electronic conducting ceramic membranes for a small-scale H<sub>2</sub> production plant. *Molecules* **2015**, *20*, 4998–5023. [[CrossRef](#)]
8. Abbas, H.F.; Daud, W.M.A.W. Hydrogen production by methane decomposition: A review. *Int. J. Hydrogen Energy* **2010**, *35*, 1160–1190. [[CrossRef](#)]
9. Wang, J.; Yu, H.; Ma, Z.; Zhou, S. Enhanced stability of CaO and/or La<sub>2</sub>O<sub>3</sub> promoted Pd/Al<sub>2</sub>O<sub>3</sub> egg-shell catalysts in partial oxidation of methane to syngas. *Molecules* **2013**, *18*, 8289–8297. [[CrossRef](#)]
10. Jiao, F.; Li, J.; Pan, X.; Xiao, J.; Li, H.; Ma, H.; Wei, M.; Pan, Y.; Zhou, Z.; Li, M.; et al. Selective conversion of syngas to light olefins. *Science* **2016**, *351*, 1065–1068. [[CrossRef](#)]
11. Ha, K.-S.; Bae, J.W.; Woo, K.-J.; Jun, K.-W. Efficient utilization of greenhouse gas in a gas-to-liquids process combined with carbon dioxide reforming of methane. *Environ. Sci. Technol.* **2010**, *44*, 1412–1417. [[CrossRef](#)] [[PubMed](#)]
12. Pakhare, D.; Spivey, J. A review of dry (CO<sub>2</sub>) reforming of methane over noble metal catalysts. *Chem. Soc. Rev.* **2014**, *43*, 7813–7837. [[CrossRef](#)] [[PubMed](#)]
13. Wang, Y.; Yao, L.; Wang, S.; Mao, D.; Hu, C. Low-temperature catalytic CO<sub>2</sub> dry reforming of methane on Ni-based catalysts: A review. *Fuel Process. Technol.* **2018**, *169*, 199–206. [[CrossRef](#)]
14. Zhao, Y.; Pan, Y.X.; Xie, Y.B.; Liu, C.J. Carbon dioxide reforming of methane over glow discharge plasma-reduced Ir/Al<sub>2</sub>O<sub>3</sub> catalyst. *Catal. Commun.* **2008**, *9*, 1558–1562. [[CrossRef](#)]
15. Singh, S.A.; Madras, G. Sonochemical synthesis of Pt, Ru doped TiO<sub>2</sub> for methane reforming. *Appl. Catal. A* **2016**, *518*, 102–114. [[CrossRef](#)]
16. Derk, A.R.; Moore, G.M.; Sharma, S.; McFarland, E.W.; Metiu, H. Catalytic dry reforming of methane on ruthenium-doped ceria and ruthenium supported on ceria. *Top. Catal.* **2014**, *57*, 118–124. [[CrossRef](#)]
17. Whang, H.S.; Choi, M.S.; Lim, J.; Kim, C.; Heo, I.; Chang, T.-S.; Lee, H. Enhanced activity and durability of Ru catalyst dispersed on zirconia for dry reforming of methane. *Catal. Today* **2017**, *293*, 122–128. [[CrossRef](#)]
18. Cai, W.; Ye, L.; Zhang, L.; Ren, Y.; Yue, B.; Chen, X.; He, H. Highly dispersed nickel-containing mesoporous silica with superior stability in carbon dioxide reforming of methane: The effect of anchoring. *Materials* **2014**, *7*, 2340–2355. [[CrossRef](#)]
19. Shang, Z.; Li, S.; Li, L.; Liu, G.; Liang, X. Highly active and stable alumina supported nickel nanoparticle catalysts for dry reforming of methane. *Appl. Catal. B* **2017**, *201*, 302–309. [[CrossRef](#)]
20. Jafarbegloo, M.; Tarlani, A.; Mesbah, A.W.; Muzart, J.; Sahebdehfar, S. NiO-MgO solid solution prepared by sol-gel method as precursor for Ni/MgO methane dry reforming catalyst: Effect of calcination temperature on catalytic performance. *Catal. Lett.* **2016**, *146*, 238–248. [[CrossRef](#)]
21. Wei, J.M.; Xu, B.Q.; Li, J.L.; Cheng, Z.X.; Zhu, Q.M. Highly active and stable Ni/ZrO<sub>2</sub> catalyst for syngas production by CO<sub>2</sub> reforming of methane. *Appl. Catal. A* **2000**, *196*, L167–L172. [[CrossRef](#)]
22. Carrara, C.; Munera, J.; Lombardo, E.A.; Cornaglia, L.M. Kinetic and stability studies of Ru/La<sub>2</sub>O<sub>3</sub> used in the dry reforming of methane. *Top. Catal.* **2008**, *51*, 98–106. [[CrossRef](#)]
23. Takanabe, K.; Nagaoka, K.; Nariai, K.; Aika, K. Influence of reduction temperature on the catalytic behavior of Co/TiO<sub>2</sub> catalysts for CH<sub>4</sub>/CO<sub>2</sub> reforming and its relation with titania bulk crystal structure. *J. Catal.* **2005**, *230*, 75–85. [[CrossRef](#)]
24. Lovell, E.C.; Scott, J.; Amal, R. Ni-SiO<sub>2</sub> catalysts for the carbon dioxide reforming of methane: Varying support properties by flame spray pyrolysis. *Molecules* **2015**, *20*, 4594–4609. [[CrossRef](#)] [[PubMed](#)]
25. Boudart, M. Catalysis by supported metals. *Adv. Catal.* **1969**, *20*, 153–166.
26. Wang, H.Y.; Ruckenstein, E. Carbon dioxide reforming of methane to synthesis gas over supported rhodium catalysts: The effect of support. *Appl. Catal. A* **2000**, *204*, 143–152. [[CrossRef](#)]
27. Fu, Q.; Weber, A.; Flytzani-Stephanopoulos, M. Nanostructured Au-CeO<sub>2</sub> catalysts for low-temperature water-gas shift. *Catal. Lett.* **2001**, *77*, 87–95. [[CrossRef](#)]
28. Kurnatowska, M.; Mista, W.; Mazur, P.; Kepinski, L. Nanocrystalline Ce<sub>1-x</sub>Ru<sub>x</sub>O<sub>2</sub>—Microstructure, stability and activity in CO and soot oxidation. *Appl. Catal. B* **2014**, *148*, 123–135. [[CrossRef](#)]

29. Devaiah, D.; Reddy, L.H.; Park, S.-E.; Reddy, B.M. Ceria-zirconia mixed oxides: Synthetic methods and applications. *Catal. Rev. Sci. Eng.* **2018**, *60*, 177–277. [[CrossRef](#)]
30. Xu, S.; Yan, X.; Wang, X. Catalytic performances of NiO-CeO<sub>2</sub> for the reforming of methane with CO<sub>2</sub> and O<sub>2</sub>. *Fuel* **2006**, *85*, 2243–2247. [[CrossRef](#)]
31. Hou, T.; Yu, B.; Zhang, S.; Xu, T.; Wang, D.; Cai, W. Hydrogen production from ethanol steam reforming over Rh/CeO<sub>2</sub> catalyst. *Catal. Commun.* **2015**, *58*, 137–140. [[CrossRef](#)]
32. Fu, Y.; Wu, Y.; Cai, W.; Yue, B.; He, Y. Promotional effect of cerium on nickel-containing mesoporous silica for carbon dioxide reforming of methane. *Sci. Chin. Chem.* **2015**, *58*, 148–155. [[CrossRef](#)]
33. Liao, Y.; He, L.; Man, C.; Chen, L.; Fu, M.; Wu, J.; Ye, D.; Huang, B. Diameter-dependent catalytic activity of ceria nanorods with various aspect ratios for toluene oxidation. *Chem. Eng. J.* **2014**, *256*, 439–447. [[CrossRef](#)]
34. Raju, G.; Devaiah, D.; Reddy, P.S.; Rao, K.N.; Reddy, B.M. Hydrogenolysis of bioglycerol to 1,2-propanediol over Ru/CeO<sub>2</sub> catalysts: Influence of CeO<sub>2</sub> characteristics on catalytic performance. *Appl. Petrochem. Res.* **2014**, *4*, 297–304. [[CrossRef](#)]
35. Li, Y.; Wei, Z.; Gao, F.; Kovarik, L.; Peden, C.H.F.; Wang, Y. Effects of CeO<sub>2</sub> support facets on VO<sub>x</sub>/CeO<sub>2</sub> catalysts in oxidative dehydrogenation of methanol. *J. Catal.* **2014**, *315*, 15–24. [[CrossRef](#)]
36. Singhanian, N.; Anumol, E.A.; Ravishankar, N.; Madras, G. Influence of CeO<sub>2</sub> morphology on the catalytic activity of CeO<sub>2</sub>-Pt hybrids for CO oxidation. *Dalton Trans.* **2013**, *42*, 15343–15354. [[CrossRef](#)] [[PubMed](#)]
37. Han, J.; Meeprasert, J.; Maitarad, P.; Nammuangruk, S.; Shi, L.; Zhang, D. Investigation of the facet-dependent catalytic performance of Fe<sub>2</sub>O<sub>3</sub>/CeO<sub>2</sub> for the selective catalytic reduction of NO with NH<sub>3</sub>. *J. Phys. Chem. C* **2016**, *120*, 1523–1533. [[CrossRef](#)]
38. Huang, H.; Dai, Q.; Wang, X. Morphology effect of Ru/CeO<sub>2</sub> catalysts for the catalytic combustion of chlorobenzene. *Appl. Catal. B* **2014**, *158*, 96–105. [[CrossRef](#)]
39. Gawade, P.; Mirkelamoglu, B.; Ozkan, U.S. The role of support morphology and impregnation medium on the water gas shift activity of ceria-supported copper catalysts. *J. Phys. Chem. C* **2010**, *114*, 18173–18181. [[CrossRef](#)]
40. Wang, F.; Li, C.; Zhang, X.; Wei, M.; Evans, D.G.; Duan, X. Catalytic behavior of supported Ru nanoparticles on the {100}, {110}, and {111} facet of CeO<sub>2</sub>. *J. Catal.* **2015**, *329*, 177–186. [[CrossRef](#)]
41. Wang, Z.L.; Feng, X.D. Polyhedral shapes of CeO<sub>2</sub> nanoparticles. *J. Phys. Chem. B* **2003**, *107*, 13563–13566. [[CrossRef](#)]
42. Wang, R.; Wang, Y.; Ren, M.; Sun, G.; Gao, D.; Chong, Y.R.C.; Li, X.; Chen, G. Effect of ceria morphology on the catalytic activity of Ru/ceria for the dehydrogenation of ammonia borane. *Int. J. Hydrogen Energy* **2017**, *42*, 6757–6764. [[CrossRef](#)]
43. Wang, Z.L. Transmission electron microscopy of shape-controlled nanocrystals and their assemblies. *J. Phys. Chem. B* **2000**, *104*, 1153–1175. [[CrossRef](#)]
44. Sayle, T.X.T.; Parker, S.C.; Sayle, D.C. Oxidising CO to CO<sub>2</sub> using ceria nanoparticles. *Phys. Chem. Chem. Phys.* **2005**, *7*, 2936–2941. [[CrossRef](#)] [[PubMed](#)]
45. Liu, L.; Yao, Z.; Deng, Y.; Gao, F.; Liu, B.; Dong, L. Morphology and crystal-plane effects of nanoscale ceria on the activity of CuO/CeO<sub>2</sub> for NO reduction by CO. *ChemCatChem* **2011**, *3*, 978–989. [[CrossRef](#)]
46. Schierbaum, K.D. Ordered ultra-thin cerium oxide overlayers on Pt(111) single crystal surfaces studied by LEED and XPS. *Surf. Sci.* **1998**, *399*, 29–38. [[CrossRef](#)]
47. YAO, H.C.; YAO, Y.F.Y. Ceria in automotive exhaust catalysts. *J. Catal.* **1984**, *86*, 254–265. [[CrossRef](#)]
48. Weber, W.H.; Bass, K.C.; McBride, J.R. Raman study of CeO<sub>2</sub>: Second-order scattering, lattice dynamics, and particle-size effects. *Phys. Rev. B* **1993**, *48*, 179–184. [[CrossRef](#)]
49. Ji, S.; Xiao, Z.; Zhang, H.; Li, L.; Li, G.; Wang, L.; Liu, G. Catalytic steam reforming of n-dodecane over high surface area Ce<sub>0.75</sub>Zr<sub>0.25</sub>O<sub>2</sub> supported Ru catalysts. *Int. J. Hydrogen Energy* **2017**, *42*, 29484–29497. [[CrossRef](#)]

**Sample Availability:** Samples of the compounds are available from the authors.



© 2019 by the authors. Licensee MDPI, Basel, Switzerland. This article is an open access article distributed under the terms and conditions of the Creative Commons Attribution (CC BY) license (<http://creativecommons.org/licenses/by/4.0/>).